OPEN

Rapid-Response Low Infrared Emission Broadband Ultrathin Plasmonic Light Absorber

Giulia Tagliabue, Hadi Eghlidi & Dimos Poulikakos

Laboratory of Thermodynamics in Emerging Technologies, Institute of Energy Technology, Department of Mechanical and Process Engineering, ETH Zürich, CH-8092 Zürich, Switzerland.

Plasmonic nanostructures can significantly advance broadband visible-light absorption, with absorber thicknesses in the sub-wavelength regime, much thinner than conventional broadband coatings. Such absorbers have inherently very small heat capacity, hence a very rapid response time, and high light power-to-temperature sensitivity. Additionally, their surface emissivity can be spectrally tuned to suppress infrared thermal radiation. These capabilities make plasmonic absorbers promising candidates for fast light-to-heat applications, such as radiation sensors. Here we investigate the light-to-heat conversion properties of a metal-insulator-metal broadband plasmonic absorber, fabricated as a free-standing membrane. Using a fast IR camera, we show that the transient response of the absorber has a characteristic time below 13 ms, nearly one order of magnitude lower than a similar membrane coated with a commercial black spray. Concurrently, despite the small thickness, due to the large absorption capability, the achieved absorbed light power-to-temperature sensitivity is maintained at the level of a standard black spray. Finally, we show that while black spray has emissivity similar to a black body, the plasmonic absorber features a very low infra-red emissivity of almost 0.16, demonstrating its capability as selective coating for applications with operating temperatures up to 400°C, above which the nano-structure starts to deform.

While light absorption in plasmonic structures was initially considered an undesired effect limiting the design of plasmonic components, it has gained significant attention in recent years due to its importance in emerging areas of technology. Nowadays, thermo-plasmonic applications range from nanoscale heat sources for sunlight vapor generators[1–3], optofluidics[4,5], cancer targeting[6] and chemistry[7], to efficient coatings for solar thermoelectrics[8,9], thermal photovoltaics[10] and radiation sensors[11].

Absorption is intrinsically related to excitation of plasmons. However, efficient narrowband as well as broadband absorption requires careful design of multi-layer structures or nano-patterned layers. For example, the exploitation of strong magnetic resonances in film-coupled plasmonic nanoantennas[12,13] leads to enhanced absorption properties as compared to those of the uncoupled nanoantenna system. Such absorbers benefit from some unique advantages: on the one hand, they have subwavelength thicknesses and therefore, very low thermal capacity as compared to conventional absorbing coatings. This guarantees their rapid thermal response and high light power-to-temperature sensitivity when exposed to light. On the other hand, their absorption spectrum could be largely tuned. This could be exploited for example in designing coatings for solar applications[14,15], where, ideally, a broadband perfect absorption is desired in the visible range while zero emissivity in the infrared regime is required to suppress thermal radiation losses.

Theoretical and experimental studies on the light-to-heat conversion capabilities of plasmonic systems have focused so far on the individual and collective response of separated plasmonic nanoantennas embedded in[16,17] or supported by a bulk dielectric material[18,19]. Although such studies markedly improved the fundamental understanding of plasmonic thermal processes at the nanoscale, only few[17,18,20] considered the thermal behavior of large-scale plasmonic systems relevant beyond nano- and microscale applications. Similarly, transient thermal studies[2,5] have rather focused on the local behavior of plasmonic nanoscale heat sources and light-to-heat conversion studies of larger-scale, optimized plasmonic coatings relevant, for example, for solar-based applications are less common.

In this paper, we study the thermal response of a broadband, multilayer plasmonic absorber, fabricated as a free-standing ultrathin membrane with an area in the order of 1 cm². Using a fast IR camera, we show that, due to its subwavelength thickness and negligible heat capacity, this plasmonic absorber has a transient response time of

less than 13 ms and an absorbed light power-to-temperature sensitivity above 2.4 * 10³ K/W. Compared to similar measurements from a commercially used black spray, our plasmonic design has almost one order of magnitude faster transient thermal response while exhibiting comparable steady-state thermal sensitivity. Furthermore, using electromagnetic simulations and thermal measurements we demonstrate that our plasmonic absorber behaves as a near-ideal selective coating for solar applications, with average absorption close to 90% in the visible and near infra-red (NIR) range (up to wavelength 1000 nm) and almost negligible emission for longer wavelengths.

Results and discussion

The schematic representation of the studied broadband plasmonic absorber membrane is given in Figure 1a. It consists of a metal-insulator metal (MIM) multilayer structure presenting a continuous
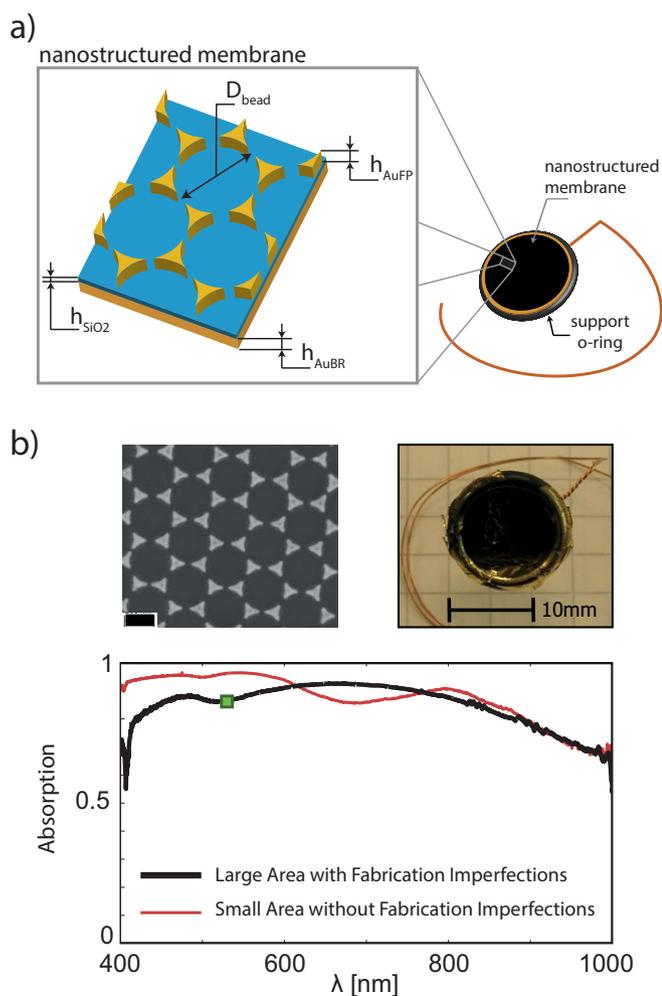

Figure 1 | Broadband Plasmonic Absorber. (a) Schematic representation of the broadband plasmonic absorber. The absorber consists of a nanostructured membrane suspended onto a thermally isolating o-ring (right). The geometrical details of the multilayer plasmonic absorber membrane are shown on the left; (b) upper panel: scanning electron micrograph from the top surface of a fabricated absorber (left, scale-bar 200 nm) and an image from an absorbing membrane suspended on an o-ring (right). Lower panel: absorption spectrum of the broadband plasmonic absorber. Red curve: absorption spectrum measured from a micrometer-scale area free of fabrication imperfections; black curve: absorption spectrum measured from a large, nanostructured area which includes standard fabrication imperfections; the green square represents the absorption at the used excitation laser wavelength.

gold back reflector ($h_{AuBR} = 100$ nm), a continuous SiO₂ dielectric layer ($h_{SiO2} = 60$ nm) and a patterned gold front layer ($h_{AuFP} = 100$ nm)[21]. The structure is realized on a glass substrate and subsequently detached and suspended on an o-ring as a thin membrane (Figure 1a, right). More details on the fabrication technique are provided in the Supplementary, S1. The continuous gold back-reflector and SiO₂ layers provide enough mechanical stability to suspend the subwavelength thin membrane. The used fabrication technique allows studying the light-to-heat conversion properties of an ultrathin plasmonic absorber on a cm²-scale and without the influence of a bulky supporting substrate.

The right inset of Figure 1b shows a picture of a free standing membrane of plasmonic absorber with diameter of 12 mm. Previously, we reported[21] large broadband absorption of a similarly structured plasmonic absorber (Figure 1b, red curve) measured from a µm² area with defect-less front pattern, as shown in the reported scanning electron micrograph (left inset of Figure 1b). Such a broad absorption spectrum was obtained exploiting simultaneously four different plasmonic resonances originating both from the front pattern geometry and its coupling to the back reflector[21]. Our large-scale (mm²-scale) absorption spectrum measurements (Figure 1b, black curve) verify that, although the absorption is reduced by a few percent in the range of 400–600 nm, similar exceptional optical properties are well preserved on a larger scale, despite the unavoidable realistic fabrication imperfections in the front array such as grain boundaries, point defects, inhomogeneities etc. Following absorption, plasmons quickly undergo non-radiative decay and the energy of the photons is converted into heat. The induced change in temperature could be exploited in a number of applications such as thermoelectric radiation sensors and solar thermal collectors. We thus performed a series of transient thermal measurements to determine the magnitude (peak temperature, T_{peak}) and the speed (characteristic time, τ) of such temperature variations. To perform transient thermal measurements we focused a continuous, green laser (wavelength 532 nm, focus size ≈0.28 mm, see Supplementary S2) at the center of the membrane (Figure 2a). With the chosen focus size we make sure that the boundaries (here the o-ring) do not affect our thermal studies. We varied the incident power, P_{inc}, from 4.8 mW to 60.3 mW using a series of neutral density filters. At this wavelength almost 85% of the incoming light power is absorbed ($P_{abs} = 0.85 * P_{inc}$, see Figure 1b). To study the transient response time, by employing a fast shutter (Figure 2a), we excited the samples with pulses of light with long enough width to ensure reaching the steady state. Furthermore, the excitation pulses have negligible rise and fall times to avoid influencing the measured temperature rise and fall times. Using an IR camera (FLIR, SC7650) we could remotely measure the temporal and spatial evolution of thermal radiation emitted from the back-side of the sample (Figure 2a). In the following, we briefly explain how the absolute temperature profiles were extracted from the IR camera images. More details could be found in Supplementary S2.

The IR camera collects thermally radiated energy in a defined wavelength range (here 3–5 µm). The collected energy consists of three contributions: the emission from the object of interest (W_{obj}), the reflected emission from ambient sources (W_{amb}) and the atmospheric emission (W_{atm}). Mathematically, this balance can be written as:

$$W_{tot}(x,y,t) = \varepsilon \tau_{air} W_{obj}(x,y,t) + (1-\varepsilon)\tau_{air} W_{amb}(x,y,t)$$
$$+ (1-\tau_{air}) W_{atm} \quad (1)$$

where ε is the emissivity of the radiating surface (here gold surface), τ_{air} is the transmittance of the atmosphere and W_{tot} is the signal recorded by the camera which has a unit of digital level, DL. Given the close distance (30 cm) between the IR camera and the sample it is safe to assume $\tau_{air} = 1$ and neglect the last (atmo-

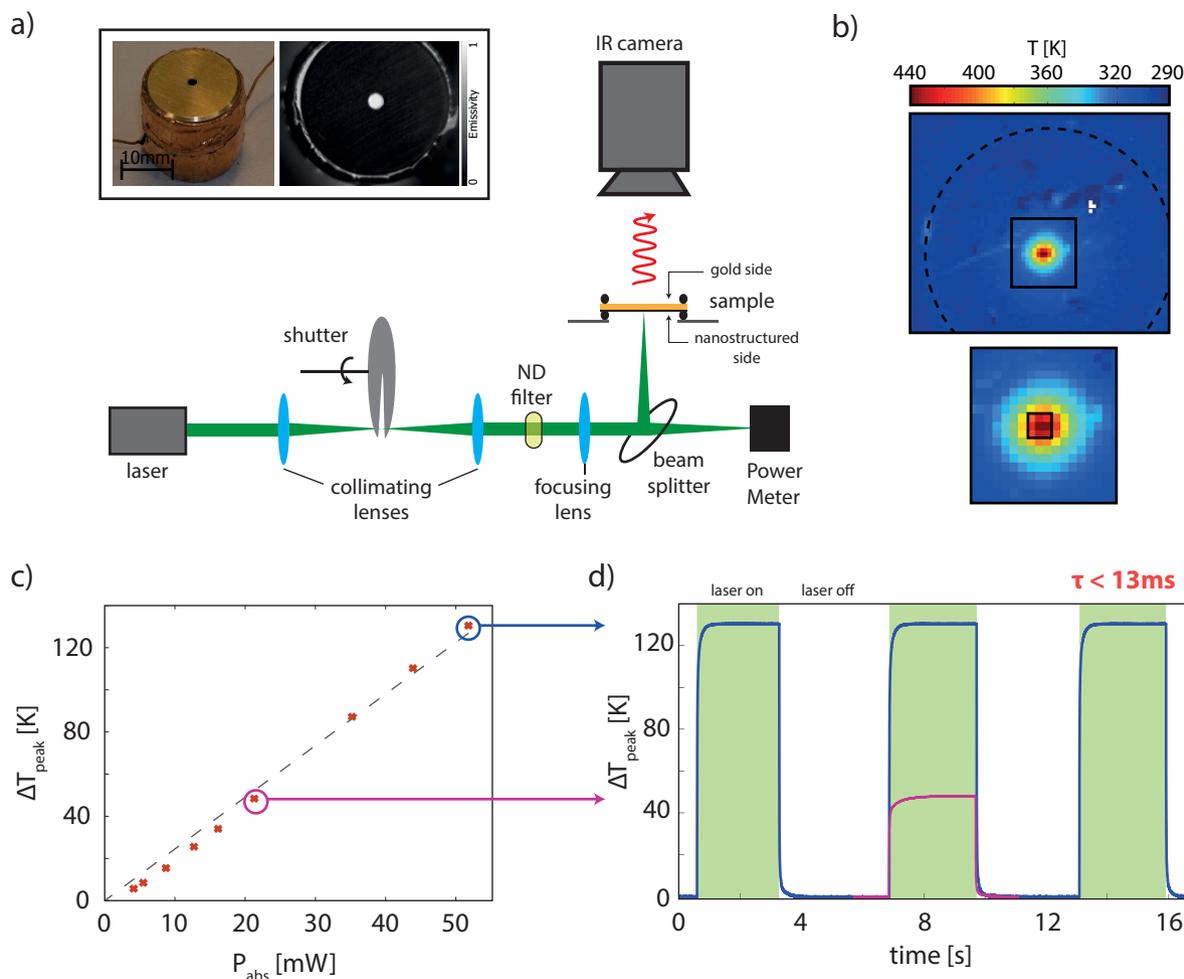Figure 2 | **IR Measurements and Characteristic Thermal Response of the Broadband Plasmonic Absorber.** (a) Schematic representation of the experimental set-up for infra-red temperature measurement. The left inset illustrates the emissivity measurement. It contains a picture of the used metallic cylinder (left) with a deep hole and the emissivity map generated by the camera software (right); (b) The upper panel contains a post-processed IR image of an absorber membrane during irradiation (the dashed circle indicates the extension of the absorber membrane). The lower panel is the zoomed view on the laser spot and the 3×3 pixel window (black square) around the hottest pixel, which are used to determine ΔT_{peak}. (c) Peak temperature increase as a function of the absorbed power. The dashed line represents a linear fit with zero intercept $\Delta T_{peak} = 2.45 * P_{abs}$. (d) Time evolution of temperature increase at maximum incident power (=60.3 mW, absorbed power =51.8 mW). The reached peak temperature determines the steady-state value of ΔT_{peak}, which is shown in (c). The purple curve shows the time evolution of temperature increase obtained for a lower incident power (=24.8 mW, absorbed power =21.3 mW).

spheric) term on the right hand side. Furthermore, we measured the emissivity of the gold surface (ε) using a black body cavity (hole with diameter-to-depth ratio higher than 10^{22}) in a metallic cylinder whose front surface is covered with gold and therefore has similar emissive characteristics to the back side of our absorber. The cylinder was electrically heated to two different temperatures. The absolute values of temperature (40°C and 60°C) were measured directly by the camera from the black body cavity assuming that the emissivity of the cavity is equal to 1. Therefore, knowing that the cylinder has uniform temperature (Biot number smaller than 0.1, see Supplementary S2), we can derive the emissivity of the gold surface (Figure 2a, left inset), which is $\varepsilon = 0.1 \pm 0.01$.

Using a black, non-reflective enclosure to isolate the system including the sample and the IR camera from the environment, we keep the reflected emission from ambient sources (background signal) constant throughout the measurement and subsequently remove its contribution by subtracting a reference frame (measured at time t = 0) from the recorded sequence. The radiation emitted from the object can be calculated as:

$$W_{obj}(x,y,t) = \frac{W_{tot}(x,y,t) - W_{tot}(x,y,0)}{\varepsilon} + W_{obj}(x,y,0) \quad (2)$$

At t = 0 the sample is in thermal equilibrium with the environment; therefore, knowing the ambient temperature and the camera calibration curve (W vs. T for a known emissivity value) we can compute $W_{obj}(x,y,0)$. Finally, the measured digital level, $W_{obj}(x,y,t)$, can be converted into temperature using the camera calibration curve which is provided by the manufacturer (see Supplementary S2 for more details). Figure 2b shows an example of a processed IR image of the sample during irradiation.

We measured the 2D temperature spatial profile every 2 ms (acquisition frequency 500 Hz). From these data we were able to extract the time evolution of the peak temperature, T_{peak}, defined as the mean temperature of a 3×3 pixels area centered around the peak position of the laser (see Figure 2b). By subtracting the ambient temperature, T_{amb}, we obtained the time variation of the temperature increase, $\Delta T_{peak} = T_{peak} - T_{amb}$, caused by the laser irradiation (Figure 2d).

The steady-state value of ΔT_{peak} (when the laser is on in Figure 2d) increases linearly with increasing irradiation power (Figure 2c), as confirmed also by numerical simulations, carried out by using COMSOL Multiphysics software (see Supplementary S3). With a laser power of approximately 60 mW we were able to obtain steady-state values of ΔT_{peak} higher than 120 K. Moreover, the high signal-to-noise ratio of the measured curve for the highest incident power (Figure 2d) allows the calculation of the system characteristic response time, defined here as the time during which ΔT_{peak} reaches from 0 to $(1-1/e)$ times of its maximum. For the case reported in Figure 2c, d, the measured value is as small as $\tau = 12.6 \pm 1.3$ ms. This short response time is attributed to the small volume of our ultra-thin system and therefore, its practically negligible heat capacity ($C_{AuBR} + C_{SiO2} \approx 4.3 \cdot 10^{-5}$ J/K).

In order to assess the thermal performance of our absorber as coating, we compare it to a typical commercial broadband black spray coating. To ensure a fair comparison of the two absorbing systems, we progressively coated one of our ultrathin absorbing membranes (Figure 3a) with a commercial black spray (*Krylon, ultra-flat black spray*). After each spraying step, we measured the characteristic temperature rise time and the steady-state ΔT_{peak} value of the membrane. By doing so, we can attribute any variation in the thermal response of the membrane solely to the effect of the black spray. For each spraying step we also estimated the area covered by the black coating. For that, we took an image of the coated sample after each spraying step and processed it with an image analysis software (*ImageJ*, see Supplementary S4 for details). In Figure 3a we started from the as-fabricated absorber (black spray area coverage equal to zero) which has a characteristic time $\tau = 10.3 \pm 0.5$ ms and increased the black spray area coverage (AC) to 16.4%, 31.9%, 35.6% and finally 80.1%. We observe that even a very discontinuous black spray coating layer with only 16.4% AC increased the response time to $\tau = 27.4 \pm 0.1$ ms. The response time increases further for higher ACs and, for the case that the surface of the sample is almost com-

pletely covered (AC = 80.1%), it reaches the value $\tau = 152 \pm 3.2$ ms, which is more than one order of magnitude larger than the response time of the bare plasmonic absorber (Figure 3a). On the other hand, the the ΔT_{peak} vs. P_{abs} curves are similar for both cases of the bare and the spray coated plasmonic absorber (Figure 3b). This similarity can be understood by considering the interplay which exists between thickness and thermal diffusivity of the layered structure. Indeed, upon increase of the sample thickness due to the black spray coating we would expect a reduction in peak temperature. However, the added spray layer has a very low thermal diffusivity ($\alpha_{spray} \sim 10^{-7}/10^{-8}$ m²/s[23], as compared to $\alpha_{gold} \sim 10^{-5}$ m²/s, $\alpha_{glass} \sim 10^{-6}$ m²/s) which improves temperature localization. At the same time, the increase in thickness and reduction in thermal diffusivity both have a detrimental effect on the transient response time, as seen in Figure 3a.

To study in a systematic manner the role of the absorber thickness on the response time and peak temperature, while excluding other physical properties such as different thermal conductivities, we varied the thicknesses of the membrane by varying the thickness of the gold back-reflector from $h_{AuBR} = 100$ nm to $h_{AuBR} = 300$ nm. Changing this dimension does not influence the optical absorption properties of the layer[21]. Figures 4a, b show that the thinnest structure outperforms the other two for both considered criteria, rise time and thermal sensitivity. To this end, the thin plasmonic absorber has the highest light-to-heat conversion efficiency with absorbed power-to-temperature sensitivity of $2.45 * 10^3$ K/W while the cases with 200 nm and 300 nm thick back reflectors have sensitivities of $1.5 * 10^3$ K/W and $1.19 * 10^3$ K/W, respectively. The thinnest absorber has also the fastest response of all, $\tau = 12.6 \pm 1.3$ ms, while the rise time increases to 17.3 ± 0.7 ms and 23 ± 2 ms for the samples with 200 nm and 300 nm thick back reflectors, respectively (here, $P_{in} = 60.3$ mW). These results are also consistent with numerical simulations (see Supplementary S3). Therefore, reducing the absorber thickness concurrently improves sensitivity and characteristic temperature rise time of the structure. To confirm the role of the patterned plasmonic surface in the high absorption properties of the
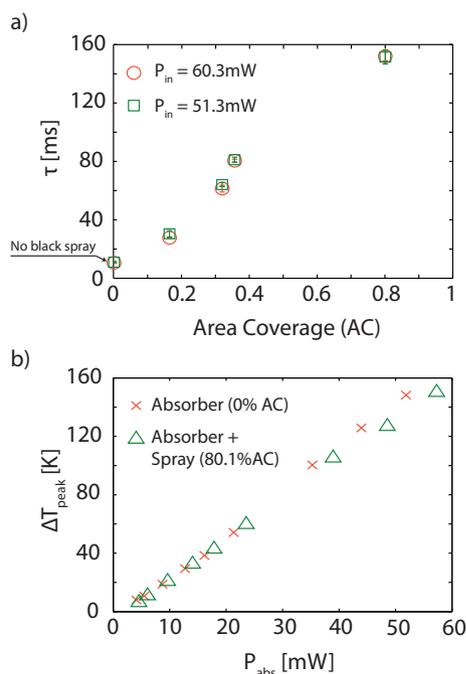

Figure 3 | Comparison of the Plasmonic Absorber with a Commercial Absorbing Coating (Black Spray). (a) Change in characteristic time with increasing area coverage (AC) of the black spray; (b) Peak steady state temperature versus absorbed power curve for the plasmonic absorber alone and the plasmonic absorber coated with black spray with area coverage of 80.1%.
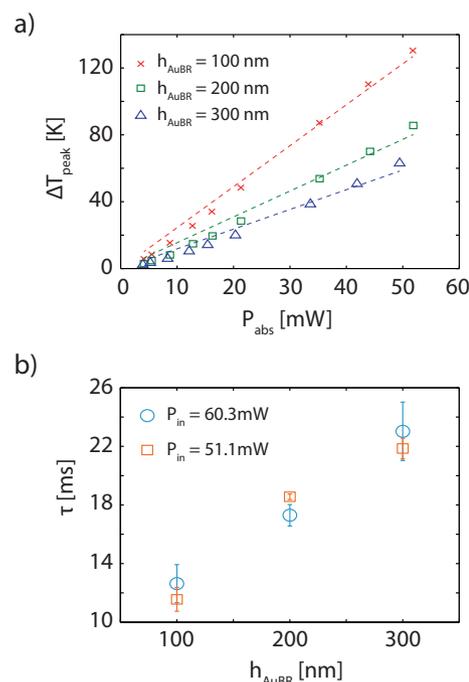

Figure 4 | Effect of Absorber Thickness. (a) Peak temperature as a function of absorbed power for samples with different thicknesses of the back reflector; (b) Characteristic time as a function of the back reflector thickness for two different incident powers.
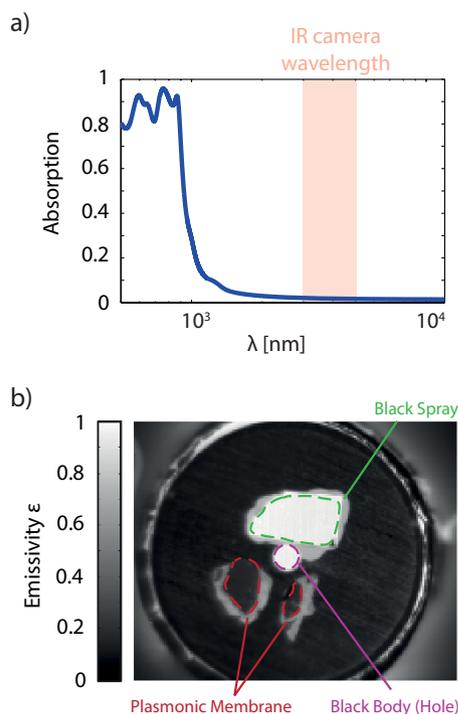
Figure 5 | Absorption and Emissivity in IR Range. (a) Simulated absorption spectrum (equivalently emissivity spectrum) of the broadband plasmonic absorber. The shaded area represents the wavelength window used by the IR camera. (b) Emissivity map measured with the IR camera in the range 3–5 μm for a membrane coated with the plasmonic absorber (dashed-red lines) and for a membrane coated with the black spray (dashed green line).

membrane, we further performed a series of control experiments on un-patterned gold membranes with different thicknesses (see Supplementary S5). These results show that large values of light power-to-temperature sensitivity can be obtained only using the nanostructured plasmonic absorber.

For applications where working temperatures are as high as a few hundreds of degrees, such as solar thermoelectrics, losses through re-emission of thermal radiation are significant and selective coatings with large absorption in the visible range but negligible emission in IR are highly desirable. We calculated the absorption coefficient of the proposed broadband plasmonic absorber across the visible and IR spectrum up to wavelength 12 μm, which corresponds to the peak emission wavelength of a black-body at 240 K (Figure 5a). The dielectric data for gold and glass were taken from literature[24,25]. Since emissivity is equal to optical absorption, Figure 5a equivalently represents the emissivity spectrum of the absorber. As shown in this figure, absorption, and therefore, thermal emissivity, drops to very small values (below 10%) for wavelengths longer than 1000 nm and is almost constant throughout the entire range measured by the camera.

Using the IR camera we were able to determine the spectrally averaged emissivity of the plasmonic absorber in the spectral range 3–5 μm. We cut small pieces of a plasmonic absorber membrane and a membrane coated with black spray and pasted them to the top facet of the metallic cylinder used for the emissivity map calculation (Figure 2a, left inset) with a thermally conductive silver paste (Figure 5b). This guarantees that the membrane pieces and the cylinder stay at the same temperature. The black-body cavity in the cylinder was used for measuring the absolute temperature. We heated up the cylinder to 41.6°C and then to 52.6°C and, by subtracting the two IR images we acquired an emissivity map of the system, which is shown in Figure 5b. We observe that while the black-spray coated

membrane has an emissivity close to unity, similar to the hole (black-body), the plasmonic absorber membrane has a much smaller emissivity $\varepsilon = 0.16 \pm 0.1$. This confirms the spectral selectivity of the plasmonic absorber. The optical properties of the designed structure strongly depend on the geometry of the front nano-pattern[21]. Therefore, the proposed absorber could be used for applications operating at temperatures up to 350–400°C, above which irreversible modifications of the triangular elements could occur[26].

Conclusion

In conclusion, we fabricated a large-scale, free-standing MIM plasmonic light absorber with subwavelength thickness and studied its light-to-heat conversion capabilities. We showed that, compared to a commercial thin-film black coating, a plasmonic absorber exhibits more than one order of magnitude faster transient response with comparable absorbed light power-to-temperature sensitivity. In particular, we studied the effect of increasing the absorber thickness and demonstrated that its ultrathin feature plays a fundamental role in determining the characteristic time response and thermal sensitivity. Furthermore, we demonstrated the spectral selectivity of our plasmonic coating and showed that it exhibits high absorption across the entire visible range but low emissivity in the IR range. Therefore, such plasmonic absorbers are excellent candidates to achieve fast and effective broadband light-to-heat conversion in a host of applications. Their exceptional optical absorption and thermal properties could be especially exploited to increase the speed of visible-light thermal sensors, as well as to improve the efficiency of solar thermoelectric devices by suppressing undesired radiation losses.

Methods

Fabrication. The structure of the absorber membrane and its fabrication steps are schematically demonstrated in Figure 1 and Supplementary Figure S1. The large scale fabrication of monolayer of polystyrene beads is achieved by a dip-coating technique: the sample is immersed in a diluted bead solution (1%wt, 10^{-3} M SDS) and withdrawn at a speed of 2.5 μm/s in a controlled atmosphere with 50% humidity.

IR Measurements. The samples are placed on an inverted microscope and excited using a green laser (wavelength 532 nm). IR measurements are performed using a low-noise, cooled IR camera (FLIR, SC7650). The details of the experimental set-up, data acquisition and calibration of the measurements are given in Figure 2 and Supplementary Information S2.

Numerical Simulations. the electrodynamic and thermodynamic simulations were both performed with COMSOL Multiphysics, which is based on the finite element method (FEM). For electrodynamic simulations, normal plane wave excitation using a port boundary condition (wavelength sweep) was used to calculate the total fields and absorption spectrum. For the thermodynamic simulations in the supplementary information S3, we used axial symmetry and reduced the problem to two dimensions. A Gaussian boundary heat source was applied with variance and total power corresponding to the experimental conditions. The thermal and optical material properties of gold and glass were taken from the literature.

1. Fang, Z. Y. *et al.* Evolution of Light-Induced Vapor Generation at a Liquid-Immersed Metallic Nanoparticle. *Nano Lett* **13**, 1736–1742, doi:Doi 10.1021/Nl4003238 (2013).
2. Neumann, O. *et al.* Solar Vapor Generation Enabled by Nanoparticles. *Acs Nano* **7**, 42–49, doi:Doi 10.1021/Nn304948h (2013).
3. Hogan, N. J. *et al.* Nanoparticles Heat through Light Localization. *Nano Lett*, doi:10.1021/nl5016975 (2014).
4. Baffou, G. & Quidant, R. Thermo-plasmonics: using metallic nanostructures as nano-sources of heat. *Laser Photonics Rev* **7**, 171–187, doi:DOI 10.1002/lpor.201200003 (2013).
5. Donner, J. S., Baffou, G., McCloskey, D. & Quidant, R. Plasmon-Assisted Optofluidics. *Acs Nano* **5**, 5457–5462, doi:Doi 10.1021/Nn200590u (2011).
6. Lukianova-Hleb, E. Y. *et al.* On-demand intracellular amplification of chemoradiation with cancer-specific plasmonic nanobubbles. *Nat Med* **20**, 778–784, doi:Doi 10.1038/Nm.3484 (2014).
7. Baffou, G. & Quidant, R. Nanoplasmonics for chemistry. *Chemical Society Reviews* **43**, 3898–3907, doi:10.1039/C3CS60364D (2014).
8. Kraemer, D. *et al.* High-performance flat-panel solar thermoelectric generators with high thermal concentration. *Nat Mater* **10**, 532–538, doi:Doi 10.1038/Nmat3013 (2011).

9. Xiong, Y. J. *et al.* Solar energy conversion with tunable plasmonic nanostructures for thermoelectric devices. *Nanoscale* **4**, 4416–4420, doi:Doi 10.1039/C2nr30208j (2012).

10. Wu, C. H. *et al.* Metamaterial-based integrated plasmonic absorber/emitter for solar thermo-photovoltaic systems. *J Optics-Uk* **14**, doi:Artn 024005 Doi 10.1088/2040-8978/14/2/024005 (2012).

11. Yi, F., Zhu, H., Reed, J. C. & Cubukcu, E. Plasmonically Enhanced Thermomechanical Detection of Infrared Radiation. *Nano Lett* **13**, 1638–1643, doi:Doi 10.1021/Nl400087b (2013).

12. Liu, N., Mesch, M., Weiss, T., Hentschel, M. & Giessen, H. Infrared Perfect Absorber and Its Application As Plasmonic Sensor. *Nano Lett* **10**, 2342–2348, doi:Doi 10.1021/Nl9041033 (2010).

13. Moreau, A. *et al.* Controlled-reflectance surfaces with film-coupled colloidal nanoantennas. *Nature* **492**, 86–+, doi:Doi 10.1038/Nature11615 (2012).

14. Sergeant, N. P., Agrawal, M. & Peumans, P. High performance solar-selective absorbers using coated sub-wavelength gratings. *Opt Express* **18**, 5525–5540 (2010).

15. Sergeant, N. P., Pincon, O., Agrawal, M. & Peumans, P. Design of wide-angle solar-selective absorbers using aperiodic metal-dielectric stacks. *Opt Express* **17**, 22800–22812 (2009).

16. Govorov, A. O. *et al.* Gold nanoparticle ensembles as heaters and actuators: melting and collective plasmon resonances. *Nanoscale Res Lett* **1**, 84–90, doi:DOI 10.1007/s11671-006-9015-7 (2006).

17. Richardson, H. H., Carlson, M. T., Tandler, P. J., Hernandez, P. & Govorov, A. O. Experimental and Theoretical Studies of Light-to-Heat Conversion and Collective Heating Effects in Metal Nanoparticle Solutions. *Nano Lett* **9**, 1139–1146, doi:Doi 10.1021/Nl8036905 (2009).

18. Baffou, G. *et al.* Photoinduced Heating of Nanoparticle Arrays. *Acs Nano* **7**, 6478–6488, doi:Doi 10.1021/Nn401924n (2013).

19. Setoura, K., Okada, Y., Werner, D. & Hashimoto, S. Observation of Nanoscale Cooling Effects by Substrates and the Surrounding Media for Single Gold Nanoparticles under CW-Laser Illumination. *Acs Nano* **7**, 7874–7885, doi:Doi 10.1021/Nn402863s (2013).

20. Virk, M., Xiong, K., Svedendahl, M., Käll, M. & Dahlin, A. B. A Thermal Plasmonic Sensor Platform: Resistive Heating of Nanohole Arrays. *Nano Lett* **14**, 3544–3549, doi:10.1021/nl5011542 (2014).

21. Tagliabue, G., Eghlidi, H. & Poulikakos, D. Facile multifunctional plasmonic sunlight harvesting with tapered triangle nanopatterning of thin films. *Nanoscale* **5**, 9957–9962, doi:Doi 10.1039/C3nr03273f (2013).

22. Campanar.P & Ricolfi, T. New Determination of Total Normal Emissivity of Cylindrical and Conical Cavities. *J Opt Soc Am* **57**, 48–&, doi:Doi 10.1364/Josa.57.000048 (1967).

23. Legaie, D. P. H., Bissieux, C. & Blain, V. Thermographic application of black coatings on metals *9th International Conference on Quantitative InfraRed Thermography (Krakow)* (2008).

24. Rakic, A. D., Djurisic, A. B., Elazar, J. M. & Majewski, M. L. Optical properties of metallic films for vertical-cavity optoelectronic devices. *Appl Optics* **37**, 5271–5283, doi:Doi 10.1364/Ao.37.005271 (1998).

25. Rubin, M. Optical-Properties of Soda Lime Silica Glasses. *Sol Energ Mater* **12**, 275–288, doi:Doi 10.1016/0165-1633(85)90052-8 (1985).

26. Tan, B. J. Y. *et al.* Fabrication of size-tunable gold nanoparticles array with nanosphere lithography, reactive ion etching, and thermal annealing. *J Phys Chem B* **109**, 11100–11109, doi:Doi 10.1021/Jp045172n (2005).

Author contribution

G.T. and H.E. conceived the idea and designed the experimental set-up. G.T. performed the experiments and the simulations. G.T., H.E. and D.P. interpreted the results. D.P. supervised all aspects of the project and gave scientific and conceptual advice. All authors contributed to writing the manuscript.

Additional information